

Mapping the Northern Galactic Disk Warp with Classical Cepheids.

D.M. Skowron¹, J. Skowron¹, P. Mróz^{1,2}, A. Udalski¹,
 P. Pietrukowicz¹, I. Soszyński¹, M.K. Szymański¹,
 R. Poleski^{1,3}, S. Kozłowski¹, K. Ulaczyk^{1,4}, K. Rybicki¹,
 P. Iwanek¹, M. Wrona¹ and M. Gromadzki¹

¹ Astronomical Observatory, University of Warsaw, Al. Ujazdowskie 4,
 00-478 Warszawa, Poland

² Division of Physics, Mathematics, and Astronomy, California Institute of Technology,
 Pasadena, CA 91125, USA

³ Department of Astronomy, Ohio State University, 140 W. 18th Ave., Columbus,
 OH 43210, USA

⁴ Department of Physics, University of Warwick, Gibbet Hill Road, Coventry,
 CV4 7AL, UK

e-mail: dszczyg@astrouw.edu.pl

ABSTRACT

We present an updated three dimensional map of the Milky Way based on a sample of 2431 classical Cepheid variable stars, supplemented with about 200 newly detected classical Cepheids from the OGLE survey. The new objects were discovered as a result of a dedicated observing campaign of the ~ 280 square degree extension of the OGLE footprint of the Galactic disk during 2018–2019 observing seasons. These regions cover the main part of the northern Galactic warp that has been deficient in Cepheids so far. We use direct distances to the sample of over 2390 classical Cepheids to model the distribution of the young stellar population in the Milky Way and recalculate the parameters of the Galactic disk warp. Our data show that its northern part is very prominent and its amplitude is $\sim 10\%$ larger than that of the southern part. By combining *Gaia* astrometric data with the Galactic rotation curve and distances to Cepheids from our sample, we construct a map of the vertical component of the velocity vector for all Cepheids in the Milky Way disk. We find large-scale vertical motions with amplitudes of 10–20 km/s, such that Cepheids located in the northern warp exhibit large positive vertical velocity (toward the north Galactic pole), whereas those in the southern warp – negative vertical velocity (toward the south Galactic pole).

Key words:

1. Introduction

The warping of the Milky Way disk has been detected with multiple tracers: 21 cm observations of neutral Hydrogen (*e.g.*, Burke 1957; Westerhout 1957; Nakanishi & Sofue 2003; Levine *et al.* 2006), distribution of dust (*e.g.*, Marshall *et al.* 2006) and stars (*e.g.*, Drimmel & Spergel 2001; Reylé *et al.* 2009; Amôres *et al.*

2017), or stellar kinematics (*e.g.*, Smart *et al.* 1998; Poggio *et al.* 2018; Romero-Gómez *et al.* 2019). However, the distances of these tracers are model-dependent. Only the studies of Galactic classical Cepheids have mapped the warp with directly measured distances to individual stars (Berdnikov 1987, Skowron *et al.* 2019, Chen *et al.* 2019, Dékány *et al.* 2019).

We know that warped stellar disks are common – over 50% of spiral galaxies experience some degree of warping (Sanchez-Saavedra *et al.* 1990), but the mechanism standing behind this phenomenon is unknown. The origin of the Milky Way warp is still debated and possible explanations can be divided in two broad classes. One possibility is that the warp formed as a result of gravitational interactions, for example, with satellite galaxies or a mis-aligned dark matter halo. Other models propose non-gravitational mechanisms such as accretion of intergalactic gas or interactions with intergalactic magnetic fields as a possible explanation of warping. See López-Corredoira (2019) and references therein. In the former models, gas as well as old and young stellar populations should be warped in a similar pattern. Alternatively, one should observe an age dependency of the Galactic warp. It is therefore important to identify individual stars of different age in the warp and measure their precise distances.

The most complete and pure sample of classical Cepheids in the Milky Way from the Optical Gravitational Lensing Experiment (OGLE) long-term sky survey (Udalski *et al.* 2018), supplemented with Cepheids from other surveys has been recently used by Skowron *et al.* (2019) to construct the most detailed 3-D map of the Galactic disk in the young stellar population, extending out to the edge of the Galaxy. The map allowed constraining the shape of the warp and the location of the line of nodes that do not match models based on other stellar populations (Romero-Gómez *et al.* 2019, Amôres *et al.* 2017).

Cepheids used by Skowron *et al.* (2019) covered the southern part of the Galactic warp (bent toward the south Galactic pole), in the Galactic longitude range $180^\circ - 360^\circ$. However, the northern side of the Milky Way warp (bent toward the north Galactic pole and located in the first Galactic quadrant, *i.e.*, $0^\circ < l < 90^\circ$), has been poorly constrained due to low number of classical Cepheids in that area. This is due to extremely high extinction close to the Galactic center and the $l < 40^\circ$ limit of the OGLE Collection of Galactic Cepheids. However, the constraints of the OGLE observing site (Las Campanas Observatory, Chile) and the OGLE telescope limitations allow obtaining reasonable photometry of Milky Way disk stars up to $l < 60^\circ$. Therefore it would be possible to extend the Cepheid sample with the first quadrant Cepheids by expanding the range of the OGLE footprint in the Galactic disk.

Knowing that the regions of high extinction in the first quadrant of the Galaxy may be too opaque for optical observations and to estimate the detectability of classical Cepheids in the OGLE extended survey, we carried out simulations in which we generated a sample of 100 000 artificial Cepheids from a 3-D distribution

based on the disk model presented by Skowron *et al.* (2019). We assigned them absolute I -band magnitudes of -3.2 and -4.8 (corresponding to the pulsation periods of 3 and 10 days, respectively; Gieren *et al.* 1998). We also used the 3-D extinction maps (Bovy *et al.* 2016) to estimate the I -band extinction toward each source. We treated a Cepheid as detected if its apparent magnitude is in the range $10.75 < I < 18.0$. Fig. 1 shows the detection probability for $M_I = -3.2$ mag (left) and $M_I = -4.8$ mag (right). The dashed line marks the original range of the OGLE survey. We see that extending the survey limit in the first Galactic quadrant, where the warping is the most significant, would ensure new detections.

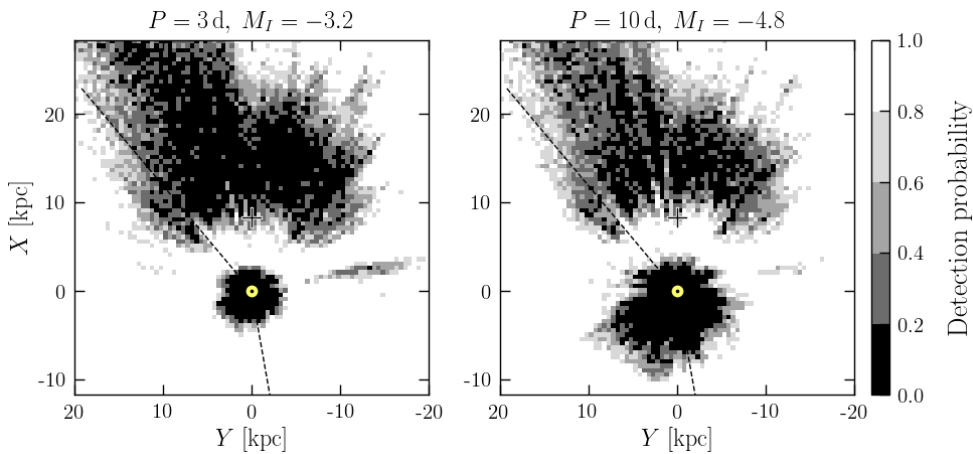


Fig. 1. The detection probability of classical Cepheids by the OGLE telescope for absolute I -band magnitudes of -3.2 (left) and -4.8 (right), corresponding to pulsation periods of 3 and 10 days, respectively. The Sun is marked with a yellow dot while the Galactic center with a cross. The dashed line marks the original range of the OGLE survey ($l < 40^\circ$ and $l > 190^\circ$).

2. Data Preparation and Analysis

2.1. Observational Data

Motivated by the outcome of the detectability simulations, the OGLE project has continued its Galaxy Variability Survey (GVS, Udalski *et al.* 2015) aiming at supplementing the OGLE Collection of Galactic Cepheids with new objects and detecting other types of variable objects in the Galactic longitude range $20^\circ < l < 60^\circ$. During the 2018 and 2019 observing seasons 201 new fields were monitored in the extended area. The number of new epochs reached 60–120 per field, depending on the location, making 122 fields suitable for the regular OGLE variability analysis. Some of these fields have additional observations from seasons 2015–2017. The process of data reduction and classical Cepheid classification in these fields was the same as in Udalski *et al.* (2018).

In the case of the remaining 79 fields the number of collected epochs was much lower – reaching 10–20 observations per field. This is not sufficient for conducting a regular OGLE variability search. Nevertheless, we attempted to extract objects which reveal light curves with an unambiguous classical Cepheid shape from the sample of clearly variable objects. The main difficulty was the estimation of the correct pulsation period based on a very small number of epochs. To make sure that our selection of classical Cepheids from these 79 fields is reliable we verified their photometry in publicly available data of the All Sky Automated Survey (ASAS; Pojmański 2002) and the Zwicky Transient Facility (ZTF; Masci *et al.* 2018), confirming most of the new candidates. Our search in these fields is in principle less complete than in the remaining parts of the sky covered by OGLE. Nevertheless, the purity of the sample should be retained.

We identified 223 classical Cepheids in the extended footprint of the OGLE GVS, of which 23 were already listed in the sample of Skowron *et al.* (2019). We cross-checked the list with other catalogs and found two on the *Gaia* Cepheid list (Holl *et al.* 2018), four in the WISE variable stars catalog (Chen *et al.* 2018) and one on the list of Chen *et al.* (2019). Fig. 2 presents the on-sky locations of classical Cepheids from the Skowron *et al.* (2019) sample (yellow and blue dots), supplemented with new detections (magenta dots), while Table 1 provides the parameters for a subset of the new list. The on-line version of the OGLE Collection of Galactic Cepheids (Udalski *et al.* 2018) has already been supplemented with the new objects.

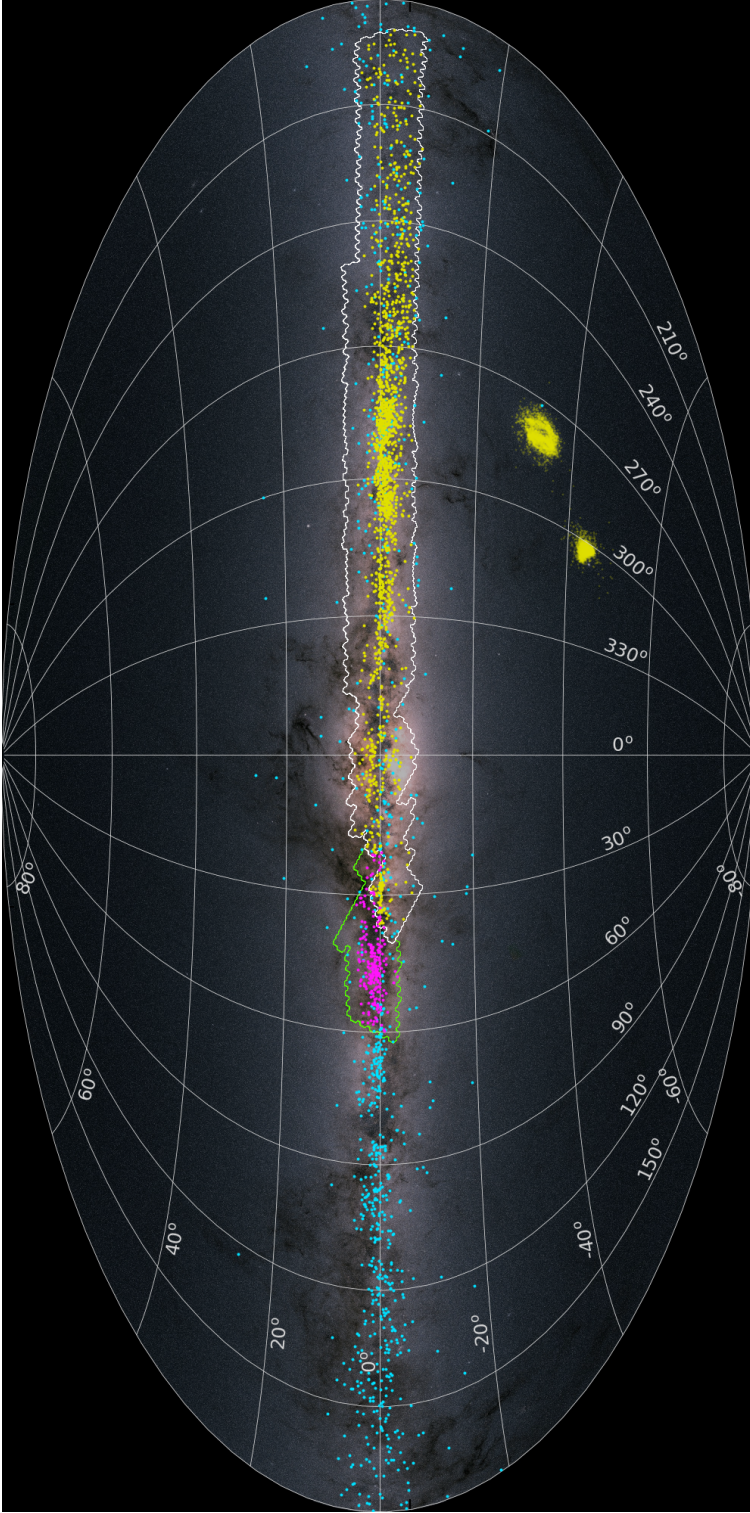


Fig. 2. The on-sky view of the Milky Way in the Galactic coordinates, on top of the Milky Way image (Credit: ESA/Gaia/DPAC, CC BY-SA 3.0 IGO¹) with all known Classical Cepheids from the OGLE collection (yellow dots) and from other surveys (cyan dots). Newly detected objects are marked with magenta dots. The total number of objects is 2632. The white contour marks the past OGLE survey footprint of the Galactic plane while the green one – the extension analyzed here².

2.2. Classical Cepheid Distances

Following the procedures described in detail in Skowron *et al.* (2019), we used the mid-infrared (mid-IR) data from *Spitzer* (Benjamin *et al.* 2003; Churchwell *et al.* 2009) and WISE (Wright *et al.* 2010; Mainzer *et al.* 2011) and the mid-IR period-luminosity (PL) relations from Wang *et al.* (2018) to calculate distances to the sample of 201 new classical Cepheids. Extinction was estimated using the extinction maps of Bovy *et al.* (2016) in the same way as in Skowron *et al.* (2019). Distances to classical Cepheids are accurate to better than 5%.

Fig. 3 shows the top view of the Milky Way with 2390 classical Cepheids that had mid-IR counterparts in the *Spitzer* and WISE catalogs. Objects from Skowron *et al.* (2019) are marked with blue dots, while newly found Cepheids with red dots. The dotted line shows the current extent of the OGLE survey (compare with Fig. 1B from Skowron *et al.* 2019). The new classical Cepheids fill an almost empty region (by far) that covers an area of the northern Galactic warp, out to the edge of the Milky Way disk.

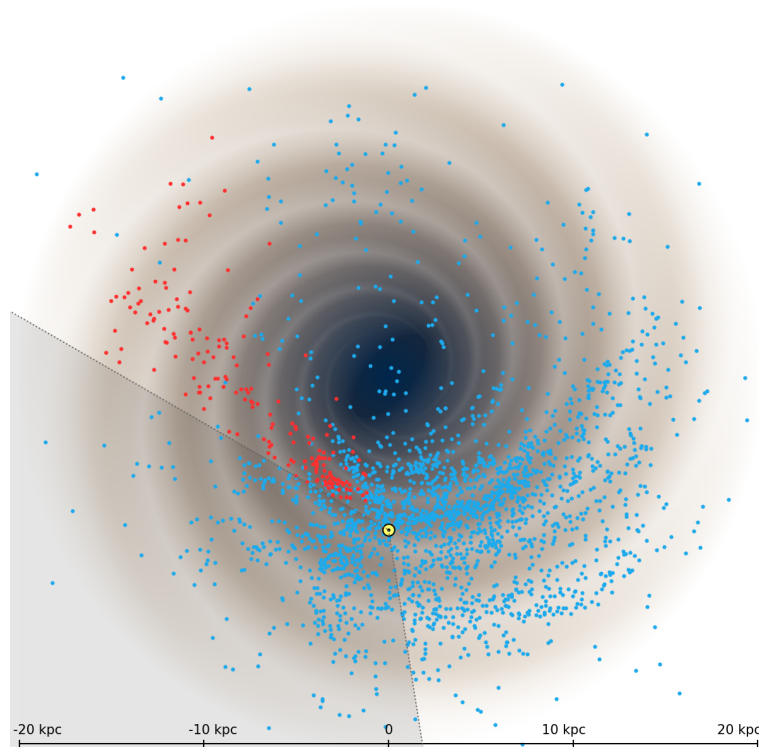


Fig. 3. Top view of the Milky Way with all 2390 Cepheids with mid-IR counterparts. The sample from Skowron *et al.* (2019) is marked with blue dots, while the newly detected objects are marked with red dots. The background image represents a four-arm spiral galaxy model consistent with neutral hydrogen measurements in our Galaxy. The Sun is marked with a yellow disk, while the dotted lines show the angular extent of the extended OGLE footprint ($l < 60^\circ$ and $l > 190^\circ$).

| Source | Cepheid ID | l [deg] | b [deg] | d [pc] | σ_d [pc] | Age [Myr] | Period [d] | F/IO | Π [mag] | Π_2 [mag] | Π_3 [mag] | Π_4 [mag] | Π_1 [mag] | Π_2 [mag] | Π_3 [mag] | Π_4 [mag] | Π_1 [mag] | Π_2 [mag] | Π_3 [mag] | Π_4 [mag] | Aks [mag] | |
|---------|-------------------|-----------|-----------|----------|-----------------|-----------|------------|------|-------------|---------------|---------------|---------------|---------------|---------------|---------------|---------------|---------------|---------------|---------------|---------------|-----------|-------|
| OGLE-1V | OGLE-GD-CER-1367 | 20.93065 | -0.56615 | 5360 | 120 | 48 | 17.4641618 | F | -7.542 | -7.515 | -7.408 | -7.384 | -7.666 | -7.588 | -7.546 | -7.546 | -7.666 | -7.588 | -7.546 | -7.546 | -7.666 | 0.821 |
| OGLE-1V | OGLE-GD-CER-1361 | 21.36920 | 1.65681 | -1 | 0 | 103 | 4.2078655 | IO | -1.000 | -1.000 | -1.000 | -1.000 | -1.000 | -1.000 | -1.000 | -1.000 | -1.000 | -1.000 | -1.000 | -1.000 | -1.000 | 0.000 |
| OGLE-1V | OGLE-GD-CER-1363 | 21.62651 | 1.17220 | -1 | 0 | 174 | 2.5083880 | F | -7.457 | -7.430 | -7.226 | -7.207 | -7.815 | -7.641 | -7.187 | -7.187 | -7.815 | -7.641 | -7.187 | -7.187 | -7.815 | 0.000 |
| OGLE-1V | OGLE-GD-CER-1364 | 21.78451 | 0.08713 | 7634 | 305 | 33 | 37.190749 | F | -1.000 | -1.000 | -1.000 | -1.000 | -1.000 | -1.000 | -1.000 | -1.000 | -1.000 | -1.000 | -1.000 | -1.000 | -1.000 | 0.000 |
| OGLE-1V | OGLE-GD-CER-1566 | 22.64006 | 1.22373 | 16804 | 1289 | 136 | 4.3574838 | F | -1.000 | -1.000 | -1.000 | -1.000 | -1.000 | -1.000 | -1.000 | -1.000 | -1.000 | -1.000 | -1.000 | -1.000 | -1.000 | 0.938 |
| OGLE-1V | OGLE-GD-CER-1374 | 22.69182 | -0.82917 | 4125 | 104 | 58 | 12.9505463 | F | 7.447 | 7.366 | 7.288 | 7.282 | 7.110 | 7.222 | 7.258 | 7.258 | 7.110 | 7.222 | 7.258 | 7.258 | 7.110 | 0.787 |
| OGLE-1V | OGLE-GD-CER-1377 | 22.96984 | 0.12494 | 3210 | 62 | 79 | 4.8895263 | IO | 7.525 | 7.493 | 7.413 | 7.374 | 7.485 | 7.420 | 7.262 | 7.262 | 7.485 | 7.420 | 7.262 | 7.262 | 7.485 | 0.420 |
| OGLE-1V | OGLE-GD-CER-1372 | 22.96984 | 0.12494 | 3210 | 62 | 79 | 4.8895263 | IO | 7.525 | 7.493 | 7.413 | 7.374 | 7.485 | 7.420 | 7.262 | 7.262 | 7.485 | 7.420 | 7.262 | 7.262 | 7.485 | 0.420 |
| ATLAS | 1279.0161-07.9499 | 24.11004 | -0.72832 | 3363 | 153 | 58 | 13.2058389 | F | 0.000 | 6.809 | 6.634 | 6.588 | 6.739 | 6.871 | 7.178 | 7.178 | 6.739 | 6.871 | 7.178 | 7.178 | 6.739 | 0.750 |
| OGLE-1V | OGLE-GD-CER-1362 | 24.22708 | 2.71716 | 23338 | 880 | 258 | 1.9732554 | IO | 13.111 | 13.195 | 12.226 | 12.969 | 13.201 | 13.587 | 0.000 | 0.000 | 13.201 | 13.587 | 0.000 | 0.000 | 13.201 | 0.460 |
| OGLE-1V | OGLE-GD-CER-1378 | 24.74936 | 0.13698 | 4661 | 126 | 58 | 12.8564317 | F | 7.818 | 7.672 | 7.509 | 7.583 | 7.794 | 7.729 | 6.457 | 6.457 | 7.794 | 7.729 | 6.457 | 6.457 | 7.794 | 1.025 |
| OGLE-1V | OGLE-GD-CER-1369 | 25.48430 | 1.58357 | 10494 | 287 | 139 | 2.5164794 | F | 11.763 | 11.624 | 11.564 | 11.587 | 11.739 | 11.845 | 1.000 | 1.000 | 11.739 | 11.845 | 1.000 | 1.000 | 11.739 | 0.741 |
| OGLE-1V | OGLE-GD-CER-1368 | 25.78035 | 1.91519 | 20438 | 1144 | 202 | 2.6340611 | F | 13.094 | 12.944 | 0.000 | 0.000 | -1.000 | -1.000 | -1.000 | -1.000 | -1.000 | -1.000 | -1.000 | -1.000 | -1.000 | 0.619 |
| OGLE-1V | OGLE-GD-CER-1365 | 26.26834 | 2.78097 | -1 | 0 | 172 | 1.7844657 | F | -1.000 | -1.000 | -1.000 | -1.000 | -1.000 | -1.000 | -1.000 | -1.000 | -1.000 | -1.000 | -1.000 | -1.000 | -1.000 | 0.000 |
| OGLE-1V | OGLE-GD-CER-1374 | 28.77625 | 2.86816 | -1 | 0 | 172 | 2.5380653 | F | -1.000 | -1.000 | -1.000 | -1.000 | -1.000 | -1.000 | -1.000 | -1.000 | -1.000 | -1.000 | -1.000 | -1.000 | -1.000 | 0.000 |
| GCVS | DV____Ser | 29.52992 | 1.40697 | 6480 | 166 | 42 | 23.1308428 | F | 7.344 | 7.335 | 7.334 | 7.249 | 7.140 | 7.194 | 7.199 | 7.199 | 7.140 | 7.194 | 7.199 | 7.199 | 7.140 | 0.422 |
| OGLE-1V | OGLE-GD-CER-1384 | 29.59993 | 1.48647 | 14376 | 452 | 114 | 4.6961076 | F | 11.414 | 11.357 | 11.296 | 11.433 | -1.000 | -1.000 | -1.000 | -1.000 | -1.000 | -1.000 | -1.000 | -1.000 | -1.000 | 0.594 |
| OGLE-1V | OGLE-GD-CER-1382 | 29.63869 | 1.97264 | 19625 | 821 | 132 | 5.0145837 | F | 12.166 | 12.033 | 11.853 | 11.817 | -1.000 | -1.000 | -1.000 | -1.000 | -1.000 | -1.000 | -1.000 | -1.000 | -1.000 | 0.685 |
| OGLE-1V | OGLE-GD-CER-1386 | 29.95373 | 1.33633 | 20479 | 521 | 90 | 6.5061474 | IO | 11.386 | 11.276 | 11.192 | 11.263 | -1.000 | -1.000 | -1.000 | -1.000 | -1.000 | -1.000 | -1.000 | -1.000 | -1.000 | 0.911 |
| OGLE-1V | OGLE-GD-CER-1376 | 30.29682 | 3.17082 | 2341 | 76 | 206 | 0.8713359 | IO | -1.000 | -1.000 | -1.000 | -1.000 | 9.441 | 9.331 | 9.339 | 9.339 | 9.441 | 9.331 | 9.339 | 9.339 | 9.441 | 0.594 |
| OGLE-1V | OGLE-GD-CER-1371 | 30.72821 | 4.15012 | 21841 | 951 | 164 | 3.3028235 | IO | -1.000 | -1.000 | -1.000 | -1.000 | 12.340 | 12.323 | 0.000 | 0.000 | 12.340 | 12.323 | 0.000 | 0.000 | 12.340 | 0.672 |
| OGLE-1V | OGLE-GD-CER-1373 | 30.75970 | 3.94171 | -1 | 0 | 86 | 8.2963145 | F | -1.000 | -1.000 | -1.000 | -1.000 | -1.000 | -1.000 | -1.000 | -1.000 | -1.000 | -1.000 | -1.000 | -1.000 | -1.000 | 0.000 |
| OGLE-1V | OGLE-GD-CER-1380 | 31.62315 | 3.58712 | 20839 | 1055 | 242 | 1.8913547 | IO | -1.000 | -1.000 | -1.000 | -1.000 | -1.000 | -1.000 | -1.000 | -1.000 | -1.000 | -1.000 | -1.000 | -1.000 | -1.000 | 0.000 |
| OGLE-1V | OGLE-GD-CER-1375 | 31.73567 | 4.17738 | 16603 | 639 | 133 | 3.0287829 | IO | -1.000 | -1.000 | -1.000 | -1.000 | 13.091 | 13.095 | 0.000 | 0.000 | 13.091 | 13.095 | 0.000 | 0.000 | 13.091 | 0.750 |
| OGLE-1V | OGLE-GD-CER-1389 | 31.89151 | 1.21029 | 14163 | 366 | 91 | 4.7349844 | IO | 11.349 | 11.260 | 0.000 | 0.000 | 11.785 | 11.778 | 0.000 | 0.000 | 11.785 | 11.778 | 0.000 | 0.000 | 11.785 | 0.524 |
| OGLE-1V | OGLE-GD-CER-1381 | 32.13330 | 3.40401 | -1 | 0 | 140 | 2.5824883 | IO | -1.000 | -1.000 | -1.000 | -1.000 | -1.000 | -1.000 | -1.000 | -1.000 | -1.000 | -1.000 | -1.000 | -1.000 | -1.000 | 1.501 |
| OGLE-1V | OGLE-GD-CER-1370 | 32.21405 | 4.99390 | 22272 | 1265 | 233 | 2.4750884 | IO | -1.000 | -1.000 | -1.000 | -1.000 | -1.000 | -1.000 | -1.000 | -1.000 | -1.000 | -1.000 | -1.000 | -1.000 | -1.000 | 0.442 |
| OGLE-1V | OGLE-GD-CER-1383 | 32.61339 | 3.35610 | -1 | 0 | 193 | 2.0885693 | F | -1.000 | -1.000 | -1.000 | -1.000 | -1.000 | -1.000 | -1.000 | -1.000 | -1.000 | -1.000 | -1.000 | -1.000 | -1.000 | 0.000 |
| OGLE-1V | OGLE-GD-CER-1398 | 32.89903 | 0.06230 | 6140 | 189 | 83 | 6.5849492 | F | 9.157 | 9.083 | 8.881 | 8.951 | -1.000 | -1.000 | -1.000 | -1.000 | -1.000 | -1.000 | -1.000 | -1.000 | -1.000 | 0.575 |
| OGLE-1V | OGLE-GD-CER-1387 | 32.98170 | 2.48250 | 20872 | 1435 | 172 | 3.6540989 | F | -1.000 | -1.000 | -1.000 | -1.000 | 12.634 | 12.677 | 0.000 | 0.000 | 12.634 | 12.677 | 0.000 | 0.000 | 12.634 | 0.818 |
| OGLE-1V | OGLE-GD-CER-1391 | 33.73762 | 1.39899 | 13922 | 663 | 111 | 4.9472037 | F | 11.622 | 11.478 | 0.000 | 0.000 | 11.265 | 11.221 | 0.000 | 0.000 | 11.265 | 11.221 | 0.000 | 0.000 | 11.265 | 0.939 |
| OGLE-1V | OGLE-GD-CER-1395 | 34.59883 | 1.41107 | 11568 | 288 | 67 | 10.8186669 | F | 10.080 | 9.962 | 0.000 | 0.000 | 10.002 | 9.932 | 9.907 | 9.907 | 10.002 | 9.932 | 9.907 | 9.907 | 10.002 | 1.095 |
| OGLE-1V | OGLE-GD-CER-1407 | 34.85424 | -0.05121 | 4091 | 108 | 51 | 17.0295145 | F | 7.424 | 7.253 | 7.136 | 7.140 | 7.234 | 7.181 | 0.000 | 0.000 | 7.234 | 7.181 | 0.000 | 0.000 | 7.234 | 1.522 |
| OGLE-1V | OGLE-GD-CER-1405 | 35.03510 | 0.33889 | 19169 | 928 | 87 | 6.6459883 | IO | 12.143 | 12.074 | 12.175 | 12.175 | -1.000 | -1.000 | -1.000 | -1.000 | -1.000 | -1.000 | -1.000 | -1.000 | -1.000 | 2.772 |
| OGLE-1V | OGLE-GD-CER-1409 | 35.51655 | 0.03691 | 5155 | 144 | 0 | 16.3873766 | F | 7.896 | 7.848 | 7.679 | 7.654 | 7.738 | 7.589 | 0.000 | 0.000 | 7.738 | 7.589 | 0.000 | 0.000 | 7.738 | 1.456 |
| OGLE-1V | OGLE-GD-CER-1388 | 35.81171 | 3.91020 | -1 | 0 | 143 | 3.4726796 | F | -1.000 | -1.000 | -1.000 | -1.000 | -1.000 | -1.000 | -1.000 | -1.000 | -1.000 | -1.000 | -1.000 | -1.000 | -1.000 | 0.000 |
| OGLE-1V | OGLE-GD-CER-1406 | 35.89617 | 0.51846 | 11064 | 761 | 113 | 2.7327063 | IO | 11.707 | 11.808 | 12.069 | 11.853 | -1.000 | -1.000 | -1.000 | -1.000 | -1.000 | -1.000 | -1.000 | -1.000 | -1.000 | 1.939 |
| OGLE-1V | OGLE-GD-CER-1390 | 36.02872 | 3.26625 | 19448 | 902 | 230 | 1.8765092 | IO | -1.000 | -1.000 | -1.000 | -1.000 | 12.767 | 12.696 | 0.000 | 0.000 | 12.767 | 12.696 | 0.000 | 0.000 | 12.767 | 0.367 |
| OGLE-1V | OGLE-GD-CER-1411 | 36.74398 | 0.44648 | 2787 | 69 | 87 | 6.6266332 | F | 7.671 | 7.529 | 7.580 | 7.544 | 7.572 | 7.437 | 7.543 | 7.543 | 7.572 | 7.437 | 7.543 | 7.543 | 7.572 | 1.054 |
| OGLE-1V | OGLE-GD-CER-1393 | 36.91397 | 2.81453 | -1 | 0 | 169 | 2.6352539 | F | -1.000 | -1.000 | -1.000 | -1.000 | -1.000 | -1.000 | -1.000 | -1.000 | -1.000 | -1.000 | -1.000 | -1.000 | -1.000 | 0.000 |
| OGLE-1V | OGLE-GD-CER-1403 | 36.92415 | 1.35472 | 13106 | 475 | 104 | 5.5286975 | F | 11.347 | 11.180 | 0.000 | 0.000 | -1.000 | -1.000 | -1.000 | -1.000 | -1.000 | -1.000 | -1.000 | -1.000 | -1.000 | 1.163 |

Table 1: The sample of newly detected classical Cepheids, sorted by Galactic longitude. The columns are as follows: 1 – The data source, 2 – Cepheid ID, 3, 4 – Galactic coordinates, 5, 6 – distance to the Cepheid and its error in pc, 7 – Cepheid age in Myr, 8 – Pulsation period in days, 9 – Pulsation mode: fundamental (F), first-overtone (IO), 10–13 – Spitzer photometry, 14–17 – WISE photometry, 18 – interstellar extinction in the Ks-band. The full Table with additional 223 classical Cepheids is available from [ftp://ogle.astrouw.edu.pl/ogle4/MILKY_WAY_3D_MAP](http://ogle.astrouw.edu.pl/ogle4/MILKY_WAY_3D_MAP)

3. Results and Discussion

3.1. The Shape of the Warp

We used the extended dataset of classical Cepheids to make an improved 3-D model of the Galactic warp. Having a more complete coverage of the far side of the disk than in Skowron *et al.* (2018) we attempted fitting the surface in the form that includes two terms of the Fourier series in the Galactocentric azimuth:

$$z(R, \phi) = \begin{cases} z_0 & \text{for } R \leq R_d \\ z_0 + z_1(R - R_d)^2 \sin(\phi - \phi_1) + z_2(R - R_d)^2 \sin 2(\phi - \phi_2) & \text{for } R > R_d \end{cases} \quad (1)$$

where z is the vertical distance from the Galactic plane, R is the distance from the Galactic center, ϕ is the Galactocentric azimuth measured counterclockwise from $l = 0^\circ$, and R_d kpc is the radius at which the disk starts warping; z_0 , z_1 , z_2 , ϕ_1 , and ϕ_2 describe the shape of the surface.

The best-fitting parameters were found by minimizing the sum

$$\chi^2 = \sum_i d_i^2 \exp(-0.5(d_i/1 \text{ kpc})^2), \quad (2)$$

where d_i is an orthogonal distance between the surface and the i th star. We multiplied the square of the distance by the exponential function to minimize the impact of outliers (the median distance d_i is 0.1 kpc). We found that the best-fit model is for:

$$\begin{aligned} R_d &= 4.2258 \pm 0.1234 \text{ kpc} \\ z_0 &= 0.0447 \pm 0.0018 \text{ kpc} \\ z_1 &= 0.0089 \pm 0.0003 \text{ kpc}^{-1} \\ \phi_1 &= 158.3^\circ \pm 0.7^\circ \\ z_2 &= 0.0022 \pm 0.0001 \text{ kpc}^{-1} \\ \phi_2 &= -13.6^\circ \pm 2.1^\circ \end{aligned}$$

The uncertainties of these quantities were estimated with a Monte Carlo simulation by drawing random heliocentric distances of Cepheids from the Gaussian distributions. It is worth noting that the lines of nodes of both terms of the Fourier series are very correlated – almost parallel.

Fig. 4 presents the new model of the Galactic warp. The disk in the center of the figure shows the top view of the Galaxy, with individual Cepheids marked with colored dots. The disk is divided into 18 regions in the Galactocentric polar coordinate system, each region being 20° wide in azimuth and marked with a different color. The vertical distribution of Cepheids within each region is shown in corresponding side panels with matching colors, where the Galactocentric distance R is plotted

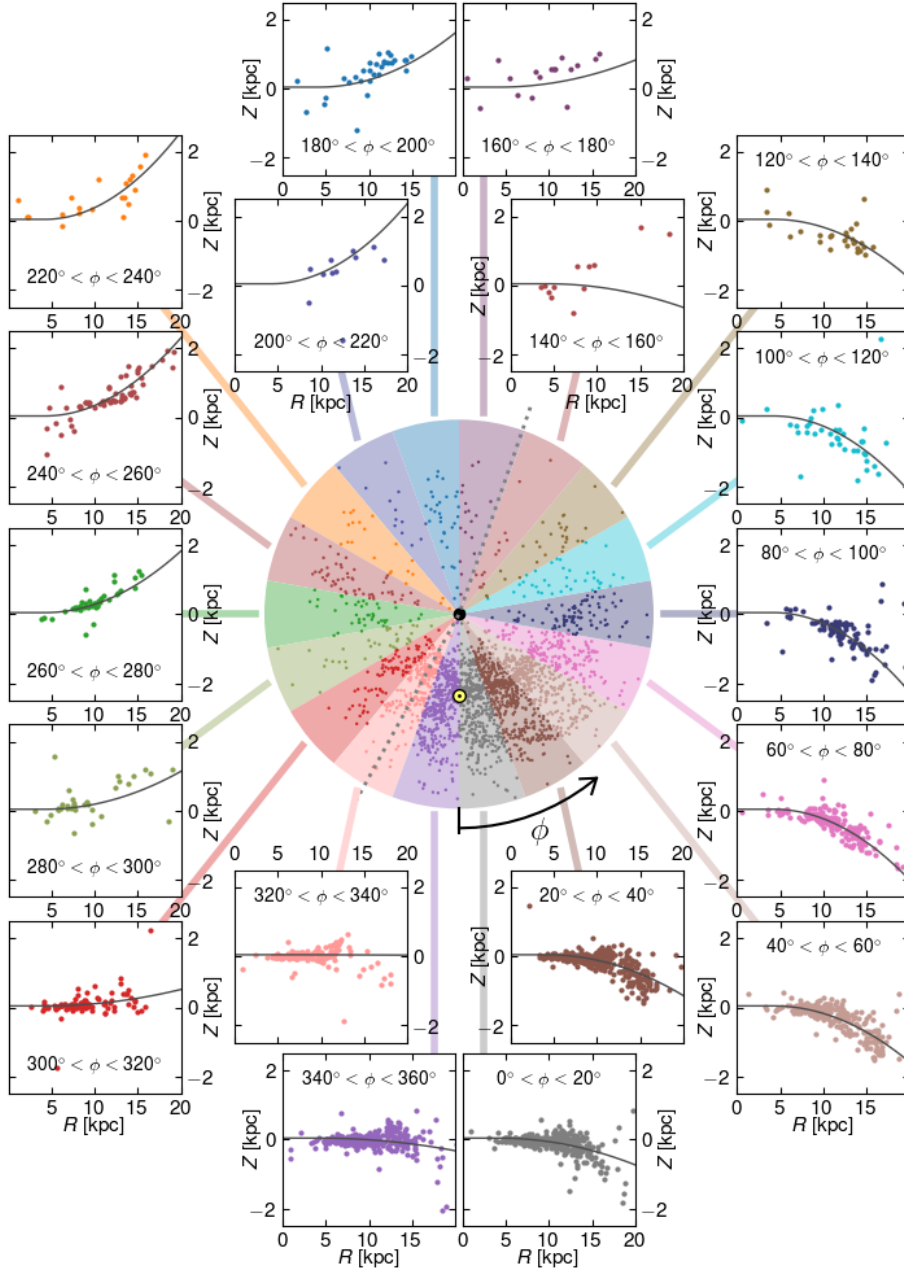


Fig. 4. The new model of the Galactic warp. The disk is divided into 18 regions in the Galactocentric polar coordinate system, marked with different colors (figure center). The Sun is marked with a yellow dot while the Galactic center with a black dot. The azimuth $\phi = 0^\circ$ is pointing toward the Sun. The dotted line divides parts of the Milky Way disk model warped south and north. The vertical distribution of Cepheids within each region is shown in corresponding panels with matching colors, where the Galactocentric distance R is plotted against distance from the Galactic plane Z . Black lines show the intersection of the median model surface within a given region.

against distance from the Galactic plane Z . Black lines show the intersection of the median model surface within a given region.

Fig. 4 shows a good agreement between the new model and the observed distribution of Cepheids. A simpler, three parameter model (where z_2 is set to zero) also provides a reasonable fit, but it cannot explain the global shape of the disk, especially in the range $90^\circ < \phi < 240^\circ$. Note that instead of using a fixed $R_d = 8$ kpc (Skowron *et al.* 2019), we leave it as a free parameter to obtain a better fit. This is now possible because the number of objects in the azimuth range $90^\circ < \phi < 270^\circ$ is sufficient.

Fig. 4 also indicates that our Cepheid sample populates all regions of the Galactic disk very well, thus presenting a complete picture of the distribution of young stars in the Milky Way, even though there are a few less populated sectors on the far side of the Galactic center, *i.e.*, $140^\circ < \phi < 160^\circ$, $160^\circ < \phi < 180^\circ$, and $200^\circ < \phi < 220^\circ$. Unfortunately, large interstellar extinction in these directions makes Cepheid detection very difficult in the optical range (see Fig. 1). In principle one could complement this sample with Cepheids detected in the infrared (IR) range, where the extinction is much lower. However, Cepheids are much more difficult to identify in the IR because their light curves are less unique and often resemble other types of variable stars. The IR sample of Cepheids based on the VISTA Variables in The Via Lactea (VVV) survey data was recently released by Dékány *et al.* (2019). We verified those objects that had counterparts in the OGLE data ($I < 19$ mag; over 300 stars) and found that only about 55% were in fact genuine Cepheids; the remaining ones ($\sim 40\%$) were eclipsing binaries or spotted stars. For this reason we decided not to include the Cepheid sample of Dékány *et al.* (2019) in our analysis.

Fig. 5 presents the best 3-D five parameter model of the Milky Way as the gray grid, with colored dots marking the positions of individual Cepheids from our sample. The viewing angles are 325° (top) and 170° (bottom), at an inclination angle 30° .

The comparison of the distribution of our Cepheid sample and the fitted model with the power law model of the Galactic warp presented by Chen *et al.* (2019) is shown in Fig. 6 for three selected non-adjacent sectors. We see that the agreement between models is reasonable in the range $30^\circ < \phi < 70^\circ$ (left panel), which is the region well populated with Cepheids in both samples. However, on the far side of the Milky Way (middle and right panels), the model of Chen *et al.* (2019) differs significantly from our model. This is not surprising because the sample of Cepheids used by Chen *et al.* (2019) to derive their models was much smaller and located mostly in the second and third Galactic quadrants, thus not covering the region of the northern Galactic warp.

Finally, the left panel of Fig. 7 shows the vertical displacement of Cepheids from the Galactic plane. Interestingly, the center of the flat part of the Galactic disk ($|Z| \simeq 0$) does not coincide with the Galactic center (black dot). If we model

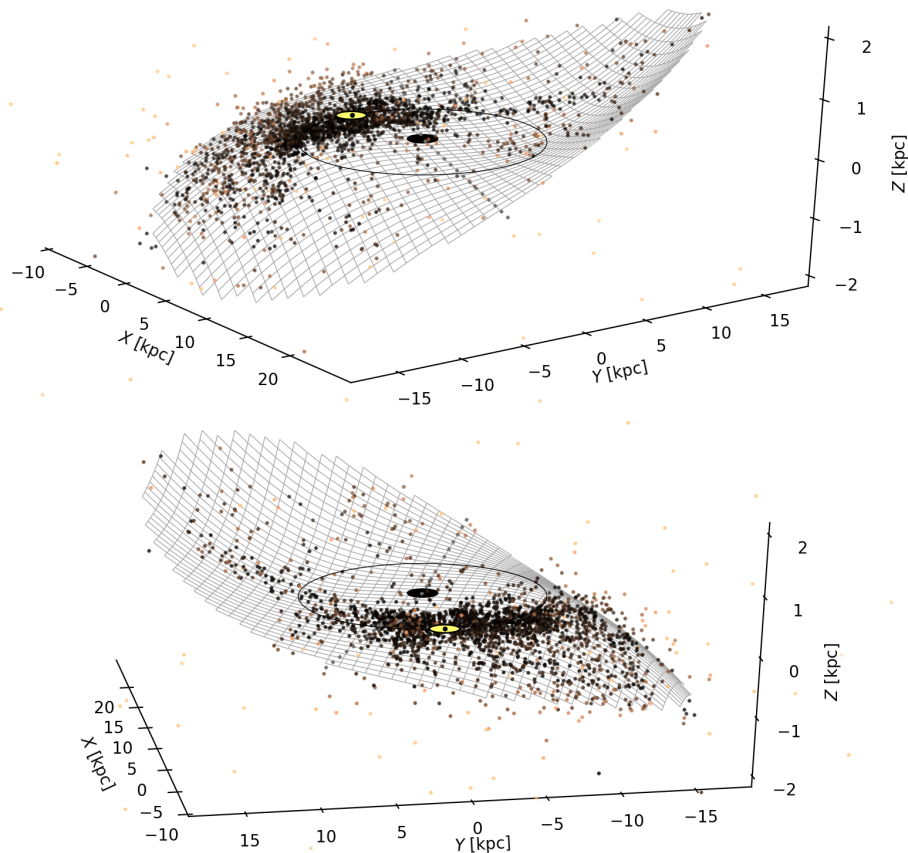


Fig. 5. Three dimensional view of the Milky Way in young stellar population. Dots mark positions of classical Cepheids from our sample. The grid represents our new model of the Galactic disk (Eq.1). The viewing angles are 325° (top) and 170° (bottom), at an inclination angle 30° . The Sun is marked with a yellow dot, while the solid line represents the solar circle. The dashed lines mark the position of the lines of nodes.

the warp with a shift of the warp center toward the Sun as a new free parameter, we find that the second term in the Fourier series (Eq. 1) is no longer necessary, while the warp center moves 2.7 kpc away from the Galactic center. The remaining parameters of the fit are: $R_d = 4.47$ kpc, $z_0 = -0.001$ kpc, $z_1 = 0.010$ kpc $^{-1}$, $\phi_1 = 159^\circ$. Allowing the fit to move in the Y direction does not produce a significantly better fit. The fact that the shift of the warp center correlates with the line connecting the Sun with the Galactic center suggests that the shift may be caused by the incompleteness of the Cepheid sample in the highly extinguished area around the Galactic center. We therefore repeated the fit after removing Cepheids that fall into the regions where their detection probability by the OGLE survey is less than 80% (gray and black area in Fig. 1). The results of the fit change only slightly, with the shift of 1.8 kpc, $R_d = 5.0$ kpc, and $\phi_1 = 163^\circ$, meaning that this is not solely a

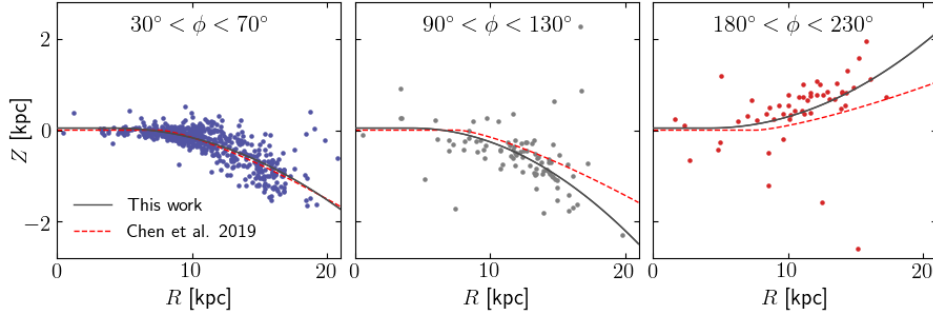


Fig. 6. The comparison of the Milky Way models from Chen *et al.* (2019) and this work for three selected regions of the Milky Way disk. The power law model of Chen *et al.* (2019) is marked with a red dashed line, while the model from this work with a gray solid line.

selection effect. The asymmetry of the S-shaped warps seems to be fairly common in simulations of warped disks caused by interactions with a satellite galaxy on a highly elongated orbit (Kim *et al.* 2014).

3.2. The Age Dependency of the Warp

The age dependence of the Milky Way warp, both in position and kinematics, has been investigated by Amôres *et al.* (2017) with the use of the 2MASS data and a population synthesis model. They found that there is a clear dependence of the thin disk scale length, warp and flare shapes with age, such that the thin disk scale length for the youngest population is twice the scale length for the oldest stars. The warping amplitude was found to be larger in the area of the northern warp for all population ages (0.5–6.0 Gyr).

Romero-Gómez *et al.* (2019) used the astrometric information from the *Gaia* Data Release 2 (DR2; *Gaia* Collaboration *et al.* 2016, 2018) to analyze the distribution of a sample of young stars (mainly OB type) and a sample of red giant branch (RGB) stars. They showed that there is the age dependency of the Galactic warp, both in position and kinematics, such that the young OB stars are less warped than the RGB stars (the height of 0.2 kpc vs. 1.0 kpc at a Galactocentric distance of 14 kpc, respectively). Also the onset radius of the warp is different for the two groups, *i.e.*, 12–13 kpc for the young stars and 10–11 kpc for the RGB stars. This suggests that the warping of the disk is more pronounced in the older populations.

Classical Cepheids are young objects, thus their distribution should be similar to that of OB stars. However, the findings of Romero-Gómez *et al.* (2019) are in contradiction to our results. We found that the onset radius of the warp for Cepheids (~ 4 kpc) is much lower than for both samples of Romero-Gómez *et al.* (2019), and the median height of Cepheids at a Galactocentric distance of 14 kpc is about 1 kpc, which is similar to the RGB sample, and clearly higher than for the OB sample.

Our data show that the northern part of the Galactic warp has a larger amplitude than the southern by about 200 pc at 14 kpc, while the RGB data in Romero-Gómez

et al. (2019) showed the opposite. On the other hand, the analysis by Amôres *et al.* (2017) confirms the asymmetry seen with classical Cepheids – with the northern warp being more pronounced than the southern, although the degree of the asymmetry is different (see Table 1 in Romero-Gómez *et al.* 2019).

It is worth noting, however, that the discussed Galactic disk models require various assumptions that may influence the final result. For example, Poggio *et al.* (2018) and Romero-Gómez *et al.* (2019) compute distances using a Bayesian estimator (and *Gaia* parallaxes) whereas Amôres *et al.* (2017) use 2MASS star counts and color–magnitude diagrams to constrain their analytical model of the warp. On the contrary, Galactic disk models based on Cepheids are free of any assumptions and rely solely on direct and accurate distances to individual stars.

3.3. The Kinematics of the Warp

In addition to the spatial 3-D distribution of classical Cepheids, kinematical data may provide useful information about the warp. Previously, Poggio *et al.* (2018) used the *Gaia* DR2 data to find a gradient of 5 – 6 km/s in the vertical velocities of upper main sequence stars and giants located from 8 to 14 kpc in Galactic radius. A similar kinematical evidence of the warp was detected by Romero-Gómez *et al.* (2019).

The warping is most likely to manifest in a component of the velocity vector perpendicular to the Galactic plane:

$$W = v_b \cos b + v_r \sin b + W_\odot,$$

where $v_b = 4.74\mu_b D$, μ_b is the proper motion in Galactic latitude, D – distance, v_r – radial velocity, and $W_\odot = 7.3$ km/s is the vertical component of the Solar velocity relative to the local standard of rest (LSR; Schönrich *et al.* 2010).

For the majority of detected Cepheids, we lack information about their radial velocities. Fortunately, the radial component can be estimated by assuming that random velocities of Cepheids are much smaller than their total velocity around the Galactic center. We assume the linear Galactic rotation velocity curve of Mróz *et al.* (2019) and convert it to the expected radial velocity by using the formalism of Reid *et al.* (2009). By comparing the estimated radial velocity and actual *Gaia* measurements for 866 objects, we find a dispersion of 18.6 km/s, which translates into the vertical velocity spread of $18.6 \text{ km/s} \times \sin b \leq 2 - 3 \text{ km/s}$.

Then, we smooth the vertical velocity distribution by calculating a median velocity within 3 kpc of 0.5×0.5 kpc wide bins (right panel of Fig. 7). The resulting map presents a complicated pattern of vertical velocities with a strong gradient in a direction perpendicular to the line of nodes of the warp. Cepheids located in the warp below the Galactic plane show large negative vertical velocity ($-20 \div -10$ km/s) whereas those located in the northern warp are moving toward the north Galactic pole (with positive vertical velocities of $10 \div 20$ km/s). Cepheids can be detected up to the edge of the Galactic disk whereas stars analyzed by Poggio

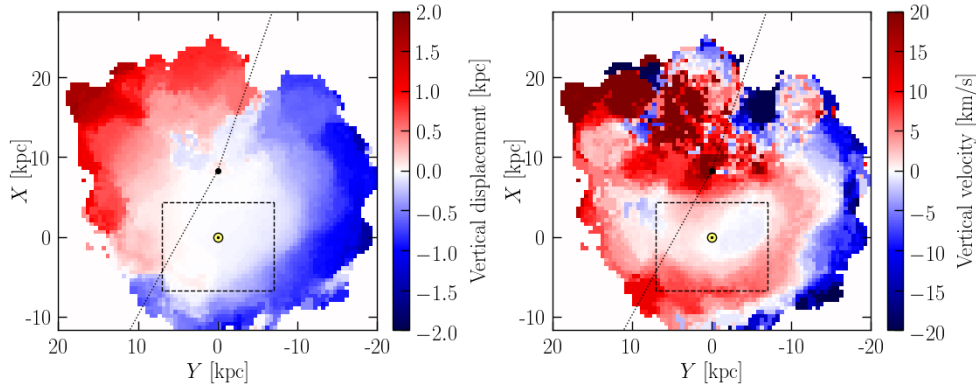


Fig. 7. The vertical distance Z from the Galactic plane (left panel) showing the extent and amplitude of the Galactic warp. The vertical velocity distribution (right panel) is smoothed by calculating a median velocity within 3 kpc of 0.5×0.5 kpc wide bins. The dotted lines represent the lines of nodes, the dashed line box shows an area investigated by Poggio *et al.* (2018). The Sun is marked with a yellow dot while the Galactic center with a black dot.

et al. (2018) are located much closer to the Sun (approximately, $-7 < X < 5$ kpc, $|Y| < 7$ kpc). In the overlapping area (the dashed line box in Fig. 7), our findings are similar to those of Poggio *et al.* (2018; see their Fig. 3CD). However, our map reveals systematic vertical motions on a much larger scale.

The vertical velocity change with the distance from the Galactic center (*i.e.*, vertical velocity waves), could be induced by the Sagittarius dwarf galaxy (Gómez *et al.* 2013) together with the vertical density waves in the Milky Way disk. The vertical velocity distribution of our Cepheid sample looks very similar, both in space and amplitude, to theoretical models (Fig. 6E of Gómez *et al.* 2013) produced by a simulation of the Sagittarius impact into the plane of the Milky Way. On the other hand, we do not observe the vertical density waves that should be phase-shifted with respect to the velocity waves.

4. Summary

We have constructed the 3-D map of the Milky Way based on classical Cepheids. The map is an update of the one presented in Skowron *et al.* (2019), supplemented with about 200 newly detected objects from the extension of the OGLE footprint in the Galactic disk, observed during the 2018 and 2019 seasons (Udalski *et al.* 2018). New Cepheids are predominantly distributed in the first Galactic quadrant – the region that was sparsely populated with Cepheids so far and that is directly opposite the region where we observe the largest bending of the Galactic disk in the southern direction (the third Galactic quadrant).

Direct distances were determined based on the mid-IR data from *Spitzer* and WISE and are accurate to better than 5%. We modeled the distribution of Cepheids with an analytic formula including two terms of the Fourier series in Galactic az-

imuth (Eq.1). We found that this model fits the entire Galactic disk very well (Fig. 4). The northern warp is very prominent and its amplitude is slightly higher than in the southern part, indicating the asymmetry of the warp.

We use *Gaia* astrometric data together with distances to Cepheids from our sample and the Galactic rotation curve to construct a map of the vertical component of the velocity vector for all Cepheids in the Milky Way disk. We find that Cepheids located in the northern warp have large positive vertical velocity (toward the north Galactic pole), while those in the southern warp – negative vertical velocity (toward the south Galactic pole). The vertical velocity amplitudes are of the order of 10–20 km/s.

Because the sample of Cepheids analyzed in this work populates almost an entire Galactic disk, there is not much room for further improvements of the model of the Galactic warp. Additional Galactic classical Cepheids can still be found in the regions of the northern sky unavailable to the OGLE survey, and with the use of infrared observations. These regions are, however, covering mostly the flat parts of the disk close to the lines of nodes of the disk model.

Acknowledgements. The OGLE project has received funding from the National Science Center (NCN) grant MAESTRO 2014/14/A/ST9/00121 to AU. This work has been supported in part by the NCN grant MAESTRO no. 2016/22/A/ST9/00009 to IS. This work has made use of data from the European Space Agency (ESA) mission *Gaia* (<https://www.cosmos.esa.int/gaia>), processed by the *Gaia* Data Processing and Analysis Consortium (DPAC, <https://www.cosmos.esa.int/web/gaia/dpac/consortium>). Funding for the DPAC has been provided by national institutions, in particular the institutions participating in the *Gaia* Multilateral Agreement.

REFERENCES

- Amôres, E. B., Robin, A. C., Reylé, C. 2017, *A&A*, **602**, A67.
 Benjamin, R. A., *et al.* 2003, *PASP*, **115**, 953.
 Berdnikov, L. N. 1987, *Pis'ma Astron. Zh.*, **13**, 45.
 Bovy, J., Rix, H.-W., Green, G. M., Schlafly, E. F., Finkbeiner, D. P. 2016, *ApJ*, **818**, 130.
 Burke, B. F. 1957, *AJ*, **62**, 90.
 Chen, X., Wang, S., Deng, L., de Grijs, R., Yang, M. 2018, *ApJS*, **237**, 28.
 Chen, X., Wang, S., Deng, L., de Grijs, R., Liu, C., Tian, H. 2019, *Nature Astronomy*, **3**, 320.
 Churchwell, E., *et al.* 2009, *PASP*, **121**, 213.
 Dékány, I., Hajdu, G., Grebel, E. K., Catelan, M. 2019, *ApJ*, **883**, 58.
 Drimmel, R., Spergel, D. N. 2001, *ApJ*, **556**, 181.
 Gaia Collaboration, Prusti, T., *et al.* 2016, *A&A*, **595**, 1.
 Gaia Collaboration, Brown, A. G. A., *et al.* 2018, *A&A*, **616**, 1.
 Gieren, W. P., Fouqué, P., Gómez, M. 1998, *ApJ*, **496**, 17.
 Gómez, F. A., Minchev, I., O'Shea, B. W., Beers, T. C., Bullock, J. S., Purcell, C. W. 2013, *MNRAS*, **429**, 159.
 Holl, B., *et al.* 2018, *A&A*, **618**, 30.
 Kim, J. H., Peirani, S., Kim, S., Ann, H. B., An, S.-H., Yoon, S.-J. 2014, *ApJ*, **789**, 90.

- Levine, E. S., Blitz, L., Heiles, C. 2006, *Science*, **312**, 1773.
- López-Corredoira, M. 2019, *arXiv*:, **1909.09815**, ..
- Mainzer, A., *et al.* 2011, *ApJ*, **731**, 53.
- Marshall, D. J., Robin, A. C., Reylé, C., Schultheis, M., Picaud, S. 2006, *A&A*, **453**, 635.
- Masci, F. J., *et al.* 2019, *PASP*, **131**, 995.
- Mróz, P., *et al.* 2019, *ApJ*, **870**, 10.
- Nakanishi, H., Sofue, Y. 2015, *PASJ*, **58**, 847.
- Poggio, E., *et al.* 2018, *MNRAS*, **481**, L21.
- Pojmański, G. 2002, *Acta Astron.*, **52**, 397.
- Reid, M. J., Menten, K. M., Zheng, X. W., *et al.* 2009, *ApJ*, **700**, 137.
- Reylé, C., Marshall, D. J., Robin, A. C., Schultheis, M. 2009, *A&A*, **495**, 819.
- Romero-Gómez, M., Mateu, C., Aguilar, L., Figueras, F., Castro-Ginard, A. 2019, *A&A*, **627**, A150.
- Sanchez-Saavedra, M. L., Battaner, E., Florido, E. 1990, *MNRAS*, **246**, 458.
- Schönrich, R., Binney, J., Dehnen, W. 2010, *MNRAS*, **403**, 1829.
- Skowron, D. M., *et al.* 2019, *Science*, **365**, 478.
- Smart, R. L., Drimmel, R., Lattanzi, M. G., Binney, J. J. 1998, *Nature*, **392**, 471.
- Udalski, A., Szymański, M. K., Szymański, G. 2015, *Acta Astron.*, **65**, 1.
- Udalski, A., *et al.* 2018, *Acta Astron.*, **68**, 315.
- Wang, S., Chen, X., de Grijs, R., Deng, L. 2018, *ApJ*, **852**, 78.
- Westerhout, G. 1957, *Bull. Astron. Inst. Neth.*, **13**, 201.
- Wright, E. L., *et al.* 2010, *AJ*, **140**, 1868.